The Output Characteristics of the Photovoltaic Array for Laser Wireless Power Transmission Within Non-Kolmogorov Turbulence considering Pointing Error

Zhenyang Xiong, Xing Du, Guoning Xu, *Senior Member, IEEE*, Hao Du, Zhongzhen Jia, Sheng Wang, Rong Cai, and Guixuan Ding

***Abstract*—This paper examines the output characteristics of the photovoltaic (PV) array in a laser wireless power transmission (LWPT) system considering atmospheric turbulence and pointing error r (r, θ). Firstly, we propose a theoretical model for studying the laser energy of each PV cell in non-Kolmogorov turbulence by introducing power in bucket (PIB). Then, to obtain the output characteristics of the PV array, we build the equivalent model based on the carrier continuity equation and bipolar transport equation. The results demonstrate that the power at the maximum power point (MPP) P_{mpp} and the system efficiency η_2 descend 50.9% and 51.5%, in the cases of r (20 mm, 45°) compared with r (0, 0), respectively, when the transmission distance is 1000 m. The variation range (5.1 V to 22.3 V) of the voltage at MPP V_{mpp} with r (10 mm, 45°) is distinctly larger than that (21.9 V to 23.2 V) with r (0, 0) when the transmission distance varies from 0 m to 2000 m. The findings of this study are valuable for the design of DC-DC converter, maximum power point tracking (MPPT) algorithm and the closed loop control circuit in LWPT system to make it efficient and stable operation.**

***Index Terms*—Laser wireless power transmission, non-kolmogorov turbulence, output characteristics, photovoltaic array, pointing error.**

I. Introduction

OVER the past decades, laser wireless power transmission (LWPT) technology (as depicted in Fig. 1), has attracted increasingly research interests as a means of supplying energy between space stations, satellites, and unmanned aerial vehicles [1], [2]. The output characteristics of the photovoltaic (PV) array, as the input source connects to the DC-DC converter, in the LWPT system have significant impact on its conversion efficiency, maximum power point tracking (MPPT)algorithm, and closed-loop control loop. Therefore, the output characteristics of the PV array, serving as the pivotal issue in LWPT, have received considerable attention [3], [4].

In practice applications, the PV array is composed by multiple PV cells to overcome the limitation of individual PV cells, which typically have insufficient output voltage and current. However, it's worth noting that the output currents of the PV cells within a series module may not match when exposed to unequal laser illumination, resulting in multiple peaks in the *P-V* curve and causing power loss. Moreover, in a conventional LWPT system, the laser beam may be affected by atmospheric turbulence, leading to spot distortion ad variations in irradiation intensity. Additionally, the pointing error is nonnegligible in tracking and aiming at the PV array installed on the dynamic target. As a consequence, the laser intensity distribution on the PV array renders more irregular, and then the output voltage and power of the PV array fluctuate more drastically, which will compromise the stability and operational security of the LWPT system. And the instability and volatility of the output voltage and power of the PV array will cause the DC-DC converter fail to achieve stable control, effective conversion, and efficient storage of the power from PV array. Thus, investigating the output characteristics and stability of the PV array in LWPT under atmospheric turbulence is crucial.

Recently, a number of studies have been done on the output characteristics of the PV cells [5], [6], [7], [8], [9], [10], [11]. He et al studied the efficiency of the GaAs PV cell with respect to wavelength, laser intensity and temperature [5]. Zhang evaluated the impacts of laser parameters and the PV cell profile on laser cells efficiencies [6]. Meng studied multi-field coupling characteristics of the PV cell under non-uniform laser beam irradiance [7]. Li analyzed the performance, in particular, the electrical efficiency of the PV cell under non-uniform and uniform distributions [8]. The previous researches on PV cells have focused on output characteristics under different conditions, but has not fully addressed the issue of non-uniform illumination causing mismatch in the PV array. A limited number of researchers

Manuscript received 26 June 2023; revised 24 August 2023; accepted 28 August 2023. Date of publication 31 August 2023; date of current version 6 October 2023. This work was supported by the Natural Science Foundation of Hainan Province under Grant 622MS105. *(Zhenyang Xiong and Xing Du are co-first authors.) (Corresponding author: Hao Du.)*

Zhenyang Xiong, Xing Du, Guoning Xu, Sheng Wang, Rong Cai, and Guixuan Ding are with the Aerospace Information Research Institute, Chinese Academy of Sciences, Beijing 100094, China, and also with the University of Chinese Academy of Sciences, Beijing 101408, China.

Hao Du is with the Aerospace Information Research Institute, Chinese Academy of Sciences, Beijing 100094, China, and also with the Key Laboratory of Earth Observation of Hainan Province, Hainan Aerospace Information Research Institute, Wenchang 571300, China (e-mail: duhao@aircas.ac.cn).

Zhongzhen Jia is with the Aerospace Information Research Institute, Chinese Academy of Sciences, Beijing 100094, China.

Digital Object Identifier 10.1109/JPHOT.2023.3310670

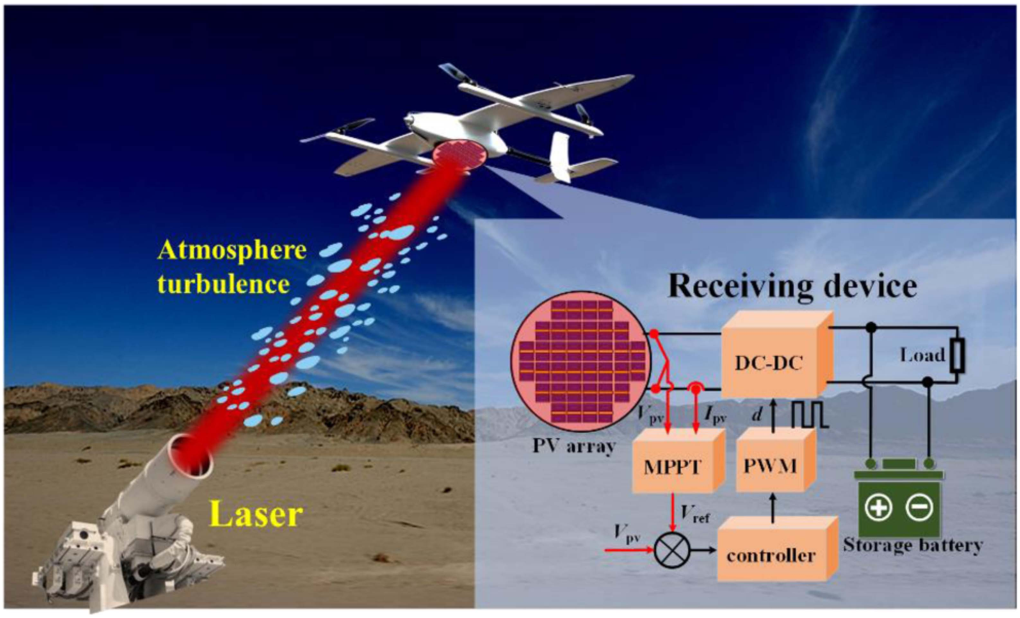

Fig. 1. Diagram of laser wireless energy transmission system in atmospheric.

have examined the effects of intensity distribution on the PV array output. Okan compared and analyzed the power, efficiency and mismatch loss of the PV array with different configurations under partial shading conditions [9]. To optimize and improve the output power and efficiency of PV array, Zhou proposed an optimal PV array configuration search mechanism for arbitrarily sized PV arrays to enhance the power under Gaussian laser beam condition [10]. However, the effects of atmospheric turbulence on the LWPT system have received comparatively little research attention. Meanwhile, the transmission characteristics of laser beams in atmospheric turbulence have been extensively studied [12], [13], [14], [15], with a particular focus on beam wander, intensity fluctuation, and spot distortion. However, the above-mentioned studies have not been applied on LWPT systems.

In this paper, we focus on the output characteristics of the PV array for LWPT within non-Kolmogorov turbulence considering pointing error and provide theoretical support for the design of the DC-DC converter, the maximum power point tracking (MPPT) algorithm and the closed loop control circuit in LWPT system, which will further enhance the output power, the laser-to-electricity conversion efficiency and the output stability of the PV array. For the propagation along the vertical path, the turbulence indicates non-Kolmogorov characters [16]. Firstly, we build the mathematical model of laser propagation by using the Huygens-Fresnel principle. Secondly, we introduce the non-Kolmogorov model, as a more general model than the Kolmogorov model, to describe atmospheric turbulence [17], [18]. Thirdly, the *I-V* characteristic equations are established by using the carrier continuity equation and bipolar transport equation. Finally, we obtain and analyze the output characteristics of the PV array on the propagation path. Our findings provide valuable insights for the optimization of the PV array structure and the laser aperture within the LWPT system, as well as the optimal system parameter range under different transmission distance and turbulence parameters is given.

The remainder of this study is structured as follows: Section II presents the analytical expressions for the average intensity, while Section III examines the numerical results. Finally, Section IV summarizes the conclusions drawn from the study.

II. Theory and Method

The laser beam propagating through non-Kolmogorov turbulence is illustrated in Fig. 2(a). Fig. 2(c) displays the changes of intensity distribution. Particularly, we present the pointing error, which is caused by the misalignment between the transmitter and receiver. Fig. 2(d) represents the power distribution of each cell considering pointing error, Fig. 2(e) shows the *I-V* and *P-V* characteristic curve of the PV array under uniform (Ir_1) and non-uniform (Ir_2, Ir_3 and Ir_4) laser irradiance. It can be seen from Fig. 2 that atmospheric turbulence and the pointing error have significant effects on the output characteristics and photoelectric conversion efficiency of the PV array.

A. Intensity Analysis of Gaussian Beam in Atmospheric Turbulence

Fig. 2 indicates that atmospheric turbulence has an impact on the light field during the laser beam propagating through the atmosphere. Accordingly, utilizing the Huygens-Fresnel principle [19], we can express the cross-spectral density function in the source plane.

$$W^{(0)}\left(\boldsymbol{\rho}_1, \boldsymbol{\rho}_2, 0\right) = \exp\left(-\frac{\boldsymbol{\rho}_1^2 + \boldsymbol{\rho}_2^2}{w_0^2}\right) \tag{1}$$

where w_0 is the waist width of GABs when $z = 0$, $\boldsymbol{\rho}_1 = (\rho_{x1}, \rho_{y1})$, $\boldsymbol{\rho}_2 = (\rho_{x2}, \rho_{y2})$.

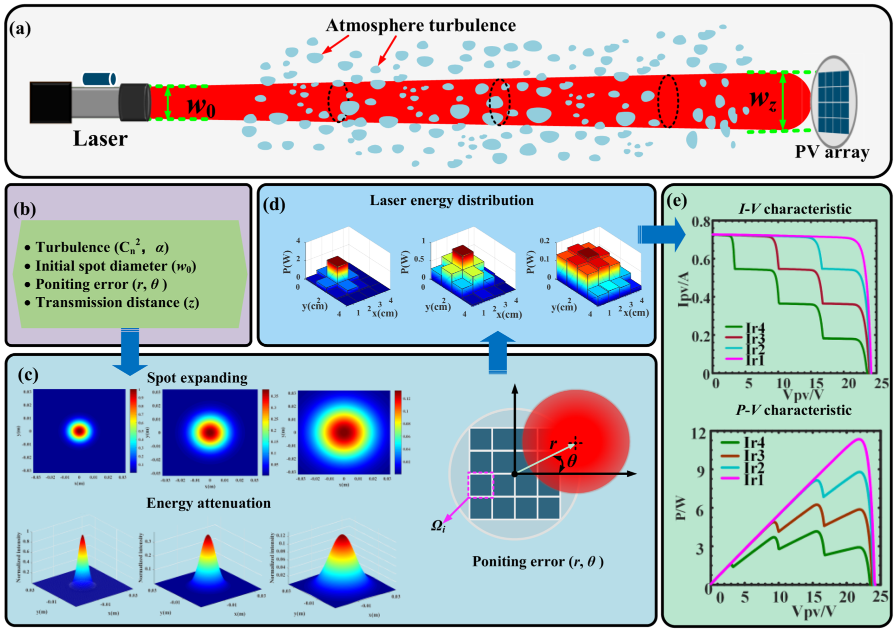

Fig. 2. Energy transmission of PV array through atmospheric turbulence.

The average intensity of laser beam propagating through non-Kolmogorov turbulence is written as

$$
\begin{aligned}
I(\boldsymbol{\rho}, z) = & \left(\frac{k}{2\pi z}\right)^2 \int\int d^2\boldsymbol{\rho}_1 \int\int d^2\boldsymbol{\rho}_2 W^{(0)}\left(\boldsymbol{\rho}_1, \boldsymbol{\rho}_2, 0\right) \\
& \times \exp\left\{\frac{ik}{2z}\left[\left(\boldsymbol{\rho}-\boldsymbol{\rho}_1\right)^2 - \left(\boldsymbol{\rho}-\boldsymbol{\rho}_2\right)^2\right]\right\} \\
& \times \left\langle \exp\left[\psi^{(a)^*}\left(\boldsymbol{\rho}, \boldsymbol{\rho}_1, z\right) + \psi^{(a)}\left(\boldsymbol{\rho}, \boldsymbol{\rho}_2, z\right)\right]\right\rangle_m
\end{aligned} \tag{2}
$$

where $\boldsymbol{\rho}_1 = (x, y)$, $k = 2\pi/\lambda$ is the wave number with wavelength λ, and $<\ldots>_{\mathrm{m}}$ represents the average over the ensemble of statistical realizations of the atmospheric turbulence, which can be expressed as [20]

$$
\begin{aligned}
& \exp\left\langle\left[\psi^{(a)*}(\boldsymbol{\rho}, \boldsymbol{\rho}_{1,z}) + \psi^{(a)}(\boldsymbol{\rho}, \boldsymbol{\rho}_{2,z})\right]\right\rangle \\
& = \exp\left\{-4\pi^2 k^2 z \int_0^1 \int_0^\infty \kappa \Phi_n(\kappa, \alpha)\right. \\
& \qquad \left. \times \left[1 - J_0(\kappa\xi|\boldsymbol{\rho}_1 - \boldsymbol{\rho}_2|)d\kappa d\xi\right]\right\}
\end{aligned} \tag{3}
$$

where J_0 (•) is the Bessel function of the first kind and order zero, $\Phi_n(\kappa, \alpha)$ is the spatial power spectrum of the refractive-index fluctuations in the atmospheric turbulence, κ is the magnitude of spatial wave number [20]. Considering the inner- and outer-scale effects, the non-Kolmogorov spectrum $\Phi_n(\kappa, \alpha)$ can be represented as [13], [14]

$$
\begin{aligned}
& \Phi_n(\kappa, \alpha) = A(\alpha) C_n^2 \exp\left(-\kappa^2/\kappa_m^2\right)\left(\kappa^2 + \kappa_0^2\right)^{-\alpha/2}, \\
& 0 < \kappa < \infty, \quad 3 < \alpha < 4,
\end{aligned} \tag{4}
$$

where $A(\alpha) = \Gamma(\alpha{-}1)\cos(\alpha\pi/2)/(4\pi^2)$, $\kappa_0 = 2\pi/L_0$, and $\kappa_m = c(\alpha)/l_0$, in which $c(\alpha) = \{\Gamma[(5{-}\alpha)/2] \cdot A(\alpha) \cdot 2\pi/3\}^{1/(\alpha-5)}$, L_0 is the outer scale and l_0 is the inner scale, α is the generalized exponent, C_n^2 is the generalized structure parameter.

By substituting (3) to (2), and after straightforward integral calculations [see Appendix], we can obtain

$$
I(\boldsymbol{\rho}, z) = \frac{\exp\left[A(z)(x^2 + y^2)\right]}{D^2(z)} \tag{5}
$$

where,

$$
A(z) = -\frac{2\left(\frac{k}{2z}\right)^2}{w_0^2\left(\frac{k}{2z}\right)^2 + \frac{1}{w_0^2} + 2\boldsymbol{I}_t} \tag{6}
$$

$$
D(z) = \sqrt{\left(\frac{k}{2z}\right)^2 + \frac{1}{w_0^4} + \frac{2}{w_0^2}\boldsymbol{I}_t} \Bigg/ \left(\frac{k}{2z}\right) \tag{7}
$$

$$
\boldsymbol{I}_t = \left\{-\frac{\pi^2 k^2 z}{3}\int_0^\infty \kappa^3 \Phi_n(\kappa, \alpha) d\kappa\right. \tag{8}
$$

B. Calculation of Laser Power

The laser power is determined by the distribution of light intensity at the corresponding area $\boldsymbol{\Omega}$. Subsequently, the expression ($p^{(\boldsymbol{\Omega})}(z)$) of the laser power received on the designated area $\boldsymbol{\Omega}$ can be calculated by means of an appropriate mathematical integral. As suggested by Siegman, the PIB is a measure of laser power focus-ability in the far field. It clearly indicates how much fraction of the total beam power is within a given bucket $\boldsymbol{\Omega}$ [21]. The PIB is defined as [22]

$$
PIB = \frac{\iint_{\boldsymbol{\Omega}} I(x, y, z) dx dy}{\iint_{\infty} I(x, y, z) dx dy} \tag{9}
$$

Then, we can obtain

$$
p^{(\boldsymbol{\Omega})}(z) = P^{(total)}(z) PIB \tag{10}
$$

where, $p^{(total)}(z)$ is the total light power, and we can obtain the total light power $p^{(total)}(z)$ at arbitrary propagation distance in (11).

$$\frac{p^{(total)}(z)}{P^{(total)}(0^+)} = \frac{\iint_\infty I(x,y,z)\mathrm{d}x\mathrm{d}y}{\iint_\infty I(x,y,0^+)\mathrm{d}x\mathrm{d}y} \tag{11}$$

Comparing (9)–(11), and we can obtain

$$p^{(\mathbf{\Omega})}(z) = P^{(total)}(0^+)\frac{\iint_{\mathbf{\Omega}} I(x,y,z)\mathrm{d}x\mathrm{d}y}{\iint_\infty I(x,y,0^+)\mathrm{d}x\mathrm{d}y} \tag{12}$$

Substituting (5) to (12), by using the integral formula in (A-6), we can obtain

$$p^{(\mathbf{\Omega})}(z) = \frac{P^{(total)}(0^+)}{\pi w_0^2/2}\iint_{\mathbf{\Omega}} I(x,y,z)\mathrm{d}x\mathrm{d}y \tag{13}$$

Assuming the area of the *i*-th PV cell is denoted as $\mathbf{\Omega}_i$. Then, considering pointing error, $\mathbf{\Omega}_i$ can be expressed as

$$\mathbf{\Omega}_i = \Big\{x_1^{(i)} - r\cos\theta \le x \le x_2^{(i)} - r\cos\theta,\; y_1^{(i)} - r\sin\theta \le x \le y_2^{(i)} - r\sin\theta\Big\} \tag{14}$$

where, the pointing error is represented as $\boldsymbol{r} = (r,\theta)$, $x_1^{(i)}$, $x_2^{(i)}$, $y_1^{(i)}$, $y_2^{(i)}$ represent the left, right, lower, upper boundaries of the region Ω_i without pointing error, respectively.

Thus, we can rewrite (13)

$$p^{(\mathbf{\Omega}_i)}(z) = \frac{P^{(total)}(0^+)}{\pi w_0^2/2}\int_{y_1^{(i)}-r\sin\theta}^{y_2^{(i)}-r\sin\theta}\int_{x_1^{(i)}-r\cos\theta}^{x_2^{(i)}-r\cos\theta} \times I(x,y,z)\mathrm{d}x\mathrm{d}y \tag{15}$$

Then, according to (6), (7), we rewrite (15)

$$p^{(\mathbf{\Omega}_i)}(z) = \frac{P^{(total)}(0^+)}{\pi w_0^2/2}\left[-\frac{\pi}{A(z)D^2(z)}\right] \times \int_{y_1^{(i)}-r\sin\theta}^{y_2^{(i)}-r\sin\theta}\int_{x_1^{(i)}-r\cos\theta}^{x_2^{(i)}-r\cos\theta}\mathrm{d}x\mathrm{d}y\left\{\frac{1}{(2\pi)\left[-1/\left(2A(z)\right)\right]} \times \exp\left[-\frac{1}{2}\left(\frac{x^2}{-1/\left(2A(z)\right)}+\frac{y^2}{-1/\left(2A(z)\right)}\right)\right]\right\} \tag{16}$$

Noting that the item in braces $\{\cdot\}$ is a two-dimensional normal distribution function with the variance ($\sqrt{-1/(2A(z))}$, $\sqrt{-1/(2A(z))}$) and mean value (0, 0). And, we denote

$$\Phi(x,y) = \frac{1}{(2\pi)\left[-1/\left(2A(z)\right)\right]}\exp\left[-\frac{1}{2}\left(\frac{x^2}{-1/\left(2A(z)\right)} + \frac{y^2}{-1/\left(2A(z)\right)}\right)\right] \tag{17}$$

Then, (16) turns into

$$p^{(\mathbf{\Omega}_i)}(z) = \frac{P^{(total)}(0^+)}{\pi w_0^2/2}\left[-\frac{\pi}{A(z)D^2(z)}\right] \int_{y_1^{(i)}-r\sin\theta}^{y_2^{(i)}-r\sin\theta}\int_{x_1^{(i)}-r\cos\theta}^{x_2^{(i)}-r\cos\theta}\Phi(x,y)\mathrm{d}x\mathrm{d}y \tag{18}$$

To perform the integral operation in (18), we introducing the cumulative distribution function (CDF) approximation function [23].

$$Q(s,t) = \{[1+\exp\left(-k(s-\mu_1)/\sigma_1\right)] \times [1+\exp\left(-k(t-\mu_2)/\sigma_2\right)]\}^{-1} \tag{19}$$

where, $\Phi(x, y)$ is the CDF of normal distribution function, which the variance and mean are $\sigma_1 = \sigma_2 = \sqrt{-1/(2A(z))}$, $\mu_1 = \mu_2 = 0$, respectively.

And we have

$$\int_{-\infty}^{t}\int_{-\infty}^{s}\Phi(x,y)dxdy \approx Q(s,t) \tag{20}$$

Then, we can obtain

$$p^{(\mathbf{\Omega}_i)}(z) = -\frac{2P^{(total)}(0^+)}{w_0^2A(z)D^2(z)}[Q(x_2^{(i)} - r\cos\theta,\; y_2^{(i)} - r\sin\theta) - Q(x_2^{(i)} - r\cos\theta,\; y_1^{(i)} - r\sin\theta) - Q(x_1^{(i)} - r\cos\theta, y_2^{(i)} - r\sin\theta\;) + Q(x_1^{(i)} - r\cos\theta, y_1^{(i)} - r\sin\theta\;)] \tag{21}$$

Based on the power distribution and the physical dimension of PV cells, the laser energy on the received plane of each PV cell can be obtained by using (21).

C. Principle and Output Characteristics of PV Cells

The equivalent circuit model of the PV cell is shown in Fig. 3(a). The *I-V* characteristic equation corresponding to the equivalent circuit model is described by (22).

$$I = I_{\mathrm{ph}} - I_{\mathrm{d1}} - I_{\mathrm{d2}} - \frac{V+IR_{\mathrm{s}}}{R_{\mathrm{sh}}} + I_{\mathrm{s-dby}} \times \left[\exp\left(\frac{V}{n_{\mathrm{dby}}V_{\mathrm{t-dby}}}\right)-1\right] \tag{22}$$

Here, I and V are the output voltage and current of the PV cell, respectively. R_{s} and R_{sh} are equivalent series and parallel parasitic resistors of PV cells. I_{d1}, I_{d2} and I_{dby} are the forward current of the diode D_1, D_2, and D_{by}, respectively. n is the diode ideal factor. I_{ph} is the photo-generated current of PV cell, which can be expressed as (23) [24].

$$I_{\mathrm{ph}} = \frac{\eta_0 P\lambda q\alpha_0^2}{hc}\mathrm{e}^{-\alpha_0 W_{\mathrm{n}}}\left(\frac{D_{\mathrm{p}}\tau_{\mathrm{p}}}{\alpha_0^2D_{\mathrm{p}}\tau_{\mathrm{p}}-1}\mathrm{e}^{\alpha_0 x_{\mathrm{n}}} + \frac{D_{\mathrm{n}}\tau_{\mathrm{n}}}{\alpha_0^2D_{\mathrm{n}}\tau_{\mathrm{n}}-1}\mathrm{e}^{-\alpha_0 x_{\mathrm{p}}}\right) \tag{23}$$

$$P = \sum_{i=1}^{4}p^{(\mathbf{\Omega}_i)}(z) \tag{24}$$

$$I_{\mathrm{d1}} = \left(qAp_{\mathrm{n0}}\sqrt{\frac{D_{\mathrm{p}}}{\tau_{\mathrm{p}}}} + qAn_{\mathrm{p0}}\sqrt{\frac{D_{\mathrm{n}}}{\tau_{\mathrm{n}}}}\right)\left[\exp\left(\frac{V+IR_{\mathrm{s}}}{n_1V_{\mathrm{t}}}\right)-1\right] \tag{25}$$

$$I_{\mathrm{d2}} = \frac{n_{\mathrm{i}}qA\left(x_{\mathrm{p}}+x_{\mathrm{n}}\right)}{2\sqrt{\tau_{\mathrm{n0}}\tau_{\mathrm{p0}}}}\left[\exp\left(\frac{V+IR_{\mathrm{s}}}{n_2V_{\mathrm{t}}}\right)-1\right] \tag{26}$$

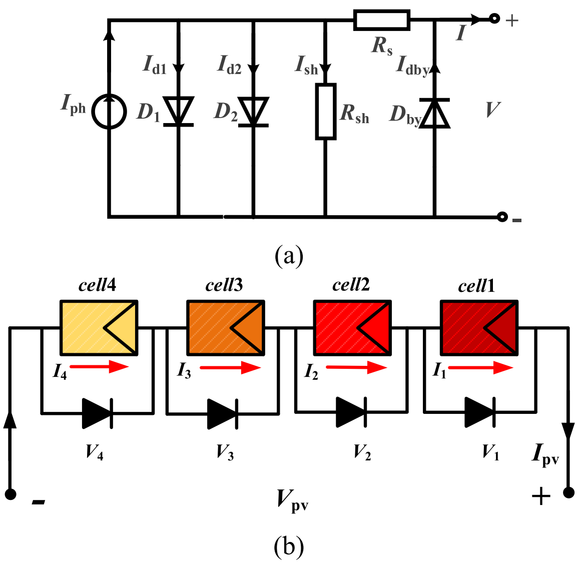

Fig. 3. Equivalent circuit model of the PV cell.

When the PV module contains N PV cells, as shown in Fig. 3(b), the output voltage V_n ($n = 1, 2, \ldots, N$) and current I_n ($n = 1, 2, \ldots, N$) of each series PV cell satisfy (22). According to the law of kirchhoff, the output I-V characteristic of the PV modules can be described as (27) when PV cells are connected in series.

$$\begin{cases} V_1 + V_2 + \ldots + V_N = V \\ I_1 (V_1) = I_2 (V_2) \\ I_1 (V_1) = I_3 (V_3) \\ \ldots \\ I_1 (V_1) = I_N (V_N) \end{cases} \tag{27}$$

In this study, the universal gallium arsenide photovoltaic cells are used to compose the PV array. The wavelength of the laser is 808nm.The specific parameters and physical constants are shown in Table 1 [24], [25].

D. PV Cells Distribution and Connection Mode in the PV Array

In this section, we present two typical and reliable connections of PV arrays in Fig. 4(a) and (b), series-parallel (SP) array and parallel-series (PS) array, respectively. To avoid the issue of multiple peaks in P-V curve mentioned above, we propose an optimal configuration design of PV array, where each PV cell in the series module receives the same irradiation power. The location of each cell in the series module is symmetrically designed with respect to the center point of laser beam considering Gaussian distribution. As shown in Fig. 4(c) and (d), the configurations of PV cells are designed for the two connection modes shown in Fig. 4(a) and (b), respectively. The number M-N in Fig. 4(c) and (d) represents the PV cell of column M and row N in Fig. 4(a) and (b).

TABLE I
UNIVERSAL GALLIUM ARSENIDE (ASGA) PHOTOVOLTAIC CELL PARAMETERS AND PHYSICAL CONSTANTS USED IN THIS PAPER

Symbol	Quantity	Value
D_n	Electron diffusion coefficients	220 cm^2/s
D_p	Hole diffusion coefficients	10.4 cm^2/s
n_i	Intrinsic carrier density	1.8×10^6 cm^{-3}
n_{p0}	Doping concentration in N region	1×10^{18} cm^{-3}
p_{n0}	Doping concentration in P region	5×10^{17} cm^{-3}
α_0	Absorption coefficient	1.4×10^4 cm^{-1}
τ_{n0}	Minority electron lifetime in the p region	10^{-9}~10^{-8} s
τ_{p0}	Minority hole lifetime in the n region	10^{-9}~10^{-8} s
x_n	Depletion width in the n region	2×10^{-9} m
x_p	Depletion width in the p region	8×10^{-9} m
W_n	Thickness of the n region	50×10^{-9} m
A	Area of photovoltaic cell	1 cm^2
$p^{(\mathrm{total})}(0^+)$	The total irradiance Power (z=0)	20 W
η_0	Photon absorption rate	90%
q	Electron charge	1.602×10^{-19} C
λ	Laser wavelength	808×10^{-9} m
c	Photon speed	3×10^8 m/s
h	Planck constant	6.63×10^{-34} J·s
k	Boltzmann constant	1.38×10^{-23} J/K
T	Cell temperature	300 K

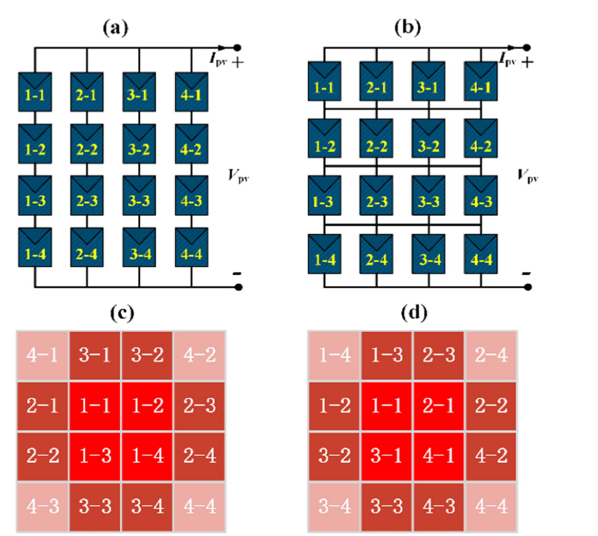

Fig. 4. Typical connections and arrangement positions of PV cells in the PV array. (a) Series-parallel connections; (b) Parallel-series connections; (c) Series-parallel arrangements; (d) Parallel-series arrangements.

III. NUMERICAL RESULTS AND DISCUSSION

A. Laser Energy Distribution on the Surface of the PV Array

The laser power distribution of each PV cell is obtained by (21), which ensures the conservation of the total power of the

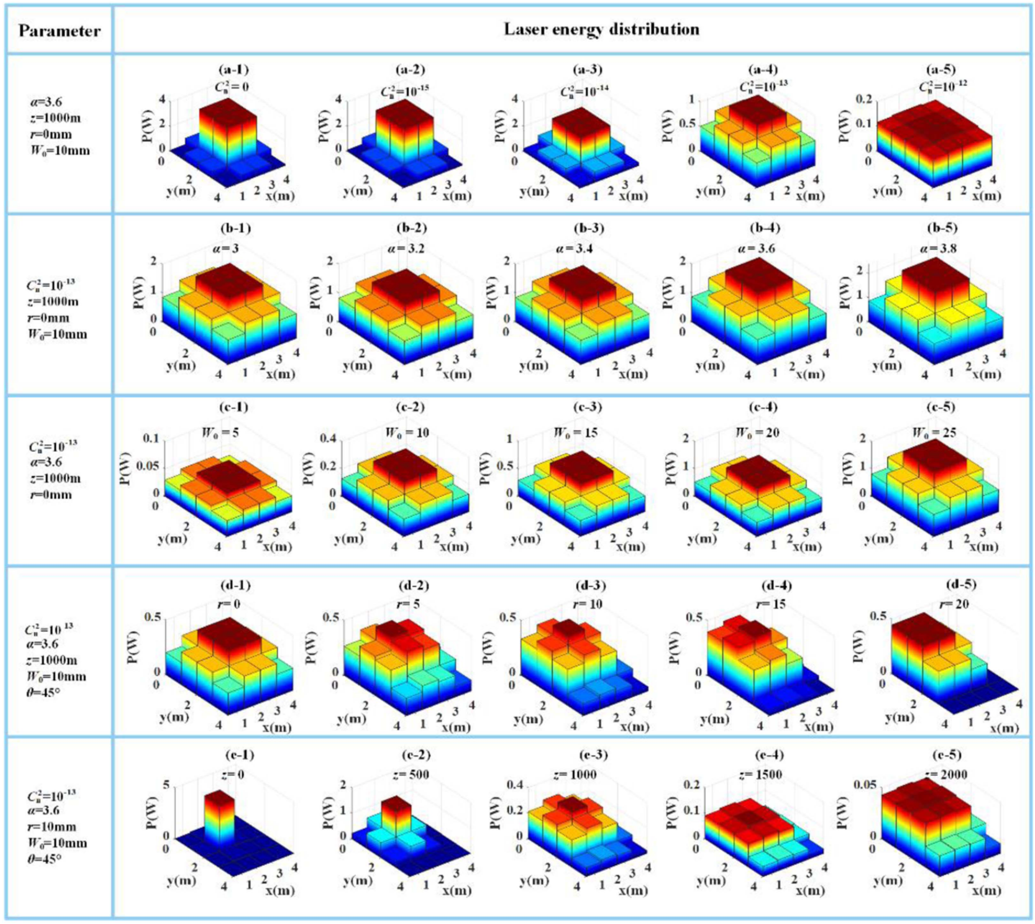

Fig. 5. Laser power distribution on each PV cell in the PV array under different parameter.

laser beam. Fig. 5 illustrates the influence of the five parameters (C_n^2, α, w_0, $\boldsymbol{r}$, z) on the power distribution of each photovoltaic cell. In Fig. 5(a-1)–(a-5), as the generalized structure parameter of atmospheric turbulence (C_n^2) increases, the overall intensity of the laser on all cells decreases, although the energy distribution tends to become more uniform among the individual cells. As shown in Fig. 5(b-1)–(b-5), the variation of the parameter α (ranging from 3 to 3.8) has a negligible effect on the laser energy distribution, while the total laser intensity on all cells reaches its minimum value when α is equal to 3.2. Fig. 5(c-1)–(c-5) illustrate that increasing the initial waist width w_0 leads to an overall increase in the total laser energy, while the two-dimensional distribution of energy remains unaltered. In Fig. 5(d-1)–(d-5), pointing error primarily affects the energy distribution of the laser by causing the peak intensity to shift from the center of the PV array to the surrounding regions. Finally, as presented in Fig. 5(e-1)–(e-5), the total laser energy decreases as the distance of laser transmission increases, leading to a more homogeneous distribution of energy on the PV cells. These results infer that the pointing error, the initial waist width w_0, propagation distance z, generalized structure parameter C_n^2, and generalized exponent α are crucial factors in determining the power distribution. Then, we carry out the output characteristics of PV array versus the mentioned parameters.

B. Effects of Atmospheric Turbulence on the Output Characteristics of the PV Array

In Section III-A, we analyzed the distribution of laser energy on the PV array under atmospheric turbulence and pointing errors. Using the equivalent circuit model and the topological structure of the PV array we obtain the *I-V* and *P-V* characteristic curves. For SP and PS arrays, the distribution of laser energy is symmetrical without pointing errors. From simulation results, we can find that the output characteristic curves of the PV arrays under SP and PS configurations are consistent. Fig. 6 shows that the output characteristics vary C_n^2, and the maximum output power and current have significant differences and attenuates as the turbulence intensity increases. As shown in Fig. 7, the turbulence generalized exponent α has weak influence on PV array output characteristics. In Fig. 8, the initial beam waist width is used to study the relationship between output characteristic curve and the size of the laser spot. The difference is less than 0.01 V in the output characteristic curve when the initial beam waist width is between 10 mm and 20 mm (accounts for 1/4 to 1/2 the side length of the PV array). The output current and power of the PV array are smaller than that of the above-mentioned condition ($w_0 = 10$, 20 mm) when the initial beam waist width is 5 mm (accounting for 1/8 of

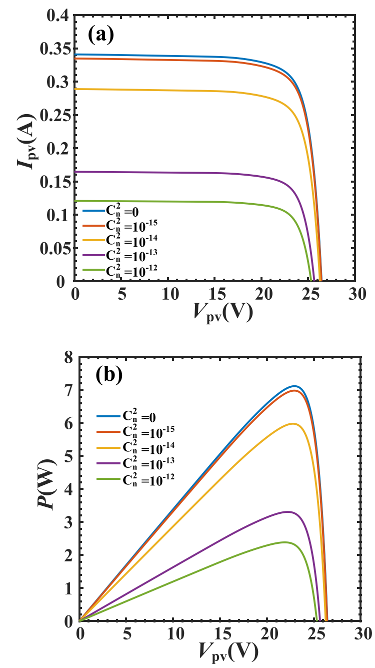

Fig. 6. Output characteristics of the PV array with turbulence power exponent $C_n^2(\mathrm{m}^{-2/3})$. Here, $w_0 = 10$ mm, $r = 0$ mm, $\alpha = 3.6$, $z = 1000$ m. (a) *I-V* curve (b) *P-V* curve.

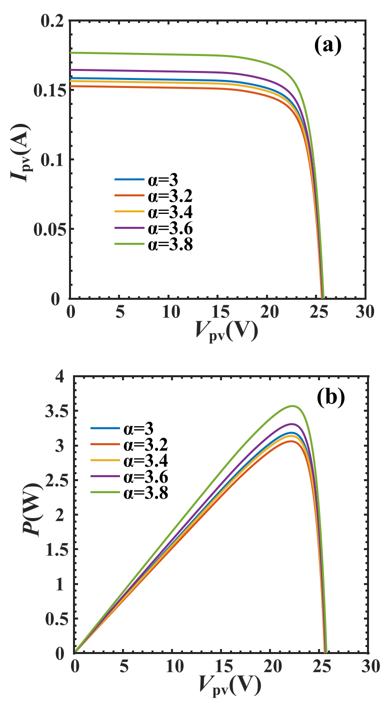

Fig. 7. Output characteristics of the PV array with refractive index structure constant α. Here, $w_0 = 10$ mm, $r = 0$ mm, $C_n^2 = 10^{-13}\mathrm{m}^{-2/3}$, $z = 1000$ m. (a) *I-V* curve (b) *P-V* curve.

the side length of the PV array and 1/2 of the PV cell). When the laser power is constant, the more concentrated the energy, the greater the irradiation intensity in per unit area. The main reason is that few PV cells in the central area of the PV array receive more laser energy. Therefore, when the strong laser irradiation

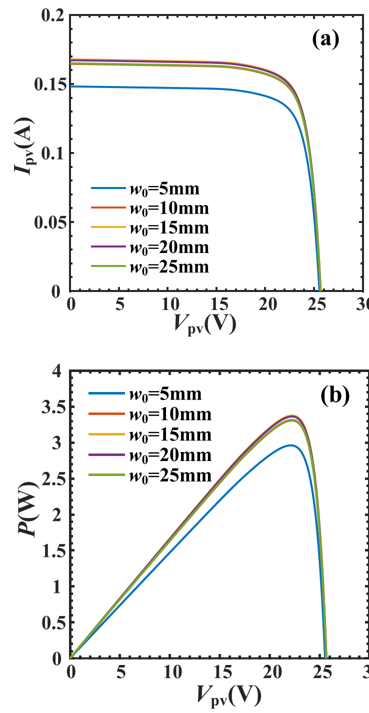

Fig. 8. Output characteristics of the PV array with initial spot diameter w_0. Here, $\alpha = 3.6$, $r = 0$ mm, $C_n^2 = 10^{-13}$ $\mathrm{m}^{-2/3}$, $z = 1000$ m. (a) *I-V* curve (b) *P-V* curve.

exceeds the maximum absorption and conversion capacity of PV cells, the remaining laser energy is converted into heat energy, resulting in power loss. The peripheral PV cells receive less intense laser irradiation, result in weaker output power. When the laser transmitting a distance of 1000 m through the atmospheric turbulence, the laser intensity of the initial beam waist width of 10 mm to 20 mm is more uniformly distributed on the PV array. Meanwhile, the laser energy can be fully absorbed and converted into electric energy by the PV cell. Therefore, when the laser power is fixed, within a certain range, the power of the LWPT system will increase with the increase of the beam waist width. However, When the beam waist is wider than the size of the PV array, the laser energy will be lost, and the overall efficiency of the system is reduced. Based on the above analysis, we can obtain that selecting an appropriate initial waist width and mitigating the pointing error represent effective strategies for enhancing the LWPT system performance.

To further analyze the impact of transmission distance and pointing errors on the output characteristics of PV cells considering atmospheric turbulence, the representative parameters are used. From Fig. 9, it can be inferred that atmospheric turbulence exerts a noticeable impact on the *I-V* characteristic curve within 1000 m. The results also suggest that pointing error significantly affects the output characteristics of the PV array, resulting in the multi-peaks *P-V* curves and attenuation of the maximum output power. Meanwhile, the voltage and current at the maximum power point will decrease obviously, which may lead to the output voltage of the DC-DC converter failing to meet the application requirements. Therefore, we assume $z = 1000$ m in the following parts. Fig. 10 illustrates the output

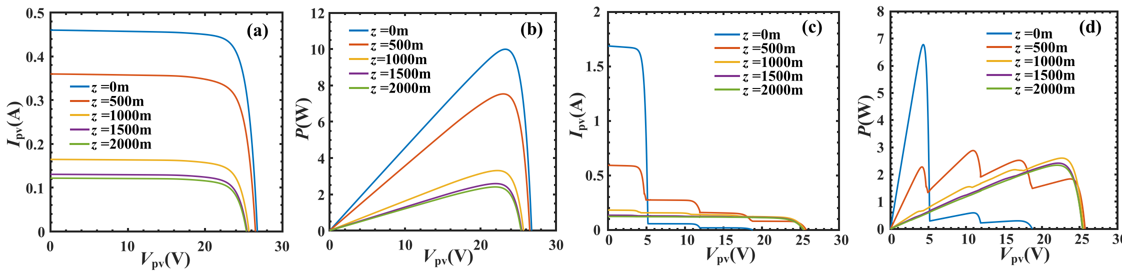

Fig. 9. Output characteristics of the PV array versus propagation distance z. Here $w_0 = 10$ mm, $C_n^2 = 10^{-13}$ m$^{-2/3}$, $\alpha = 3.6$. Here, (a), (b) are the *I-V* and *P-V* curves when $\boldsymbol{r} = \mathbf{0}$, respectively; (c), (d) are the *I-V* and *P-V* curves when $r = 10$ mm, $\theta = 45°$.

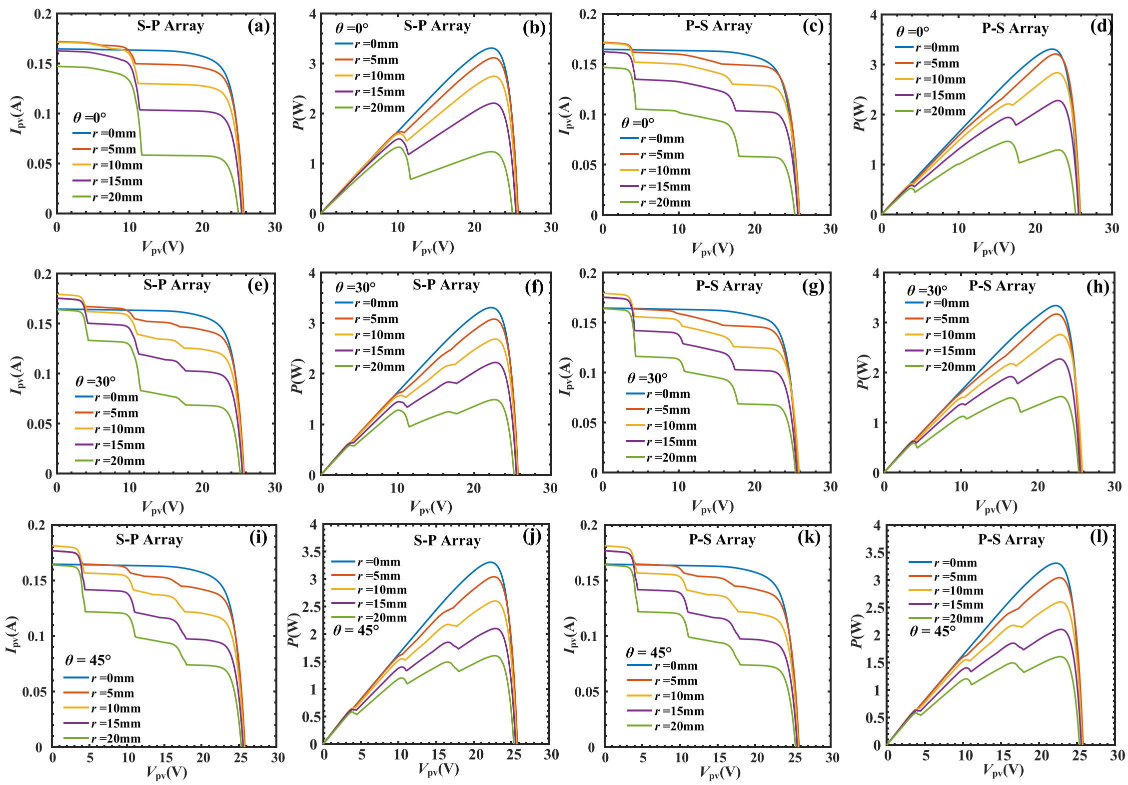

Fig. 10. Output characteristics of the PV array versus (r, θ). Here, $w_0 = 10$ mm, $C_n^2 = 10^{-13}$ m$^{-2/3}$, $\alpha = 3.6$, $z = 1000$ m.

characteristic curves of the PV array versus pointing error $\boldsymbol{r} = (r, \theta)$. Results show that when the point error $\boldsymbol{r}$ aligns with the diagonal of the square PV array, the output characteristics of SP and PS arrays are identical. When the pointing error $\boldsymbol{r}$ is symmetrical about the diagonal of the square photovoltaic cell, the output characteristics of SP or PS PV arrays are consistent with themselves but differ from each other. From Fig. 10, it can be seen that at an affirmatory θ (angle of pointing error), the *I-V* characteristic curve of the PV array presents more steps with the increase of r (distance of pointing error), and the *P-V* curve has more peaks. The output power of the PV array decreases obviously and the difficulty of MPPT algorithm to search the maximum power point increases, which will significantly reduce the stability and efficiency of the LWPT system.

C. The Maximum Power Point and Efficiencies

According to the numerical results in Section III-B, we can obtain the output voltage (V_{mpp}) and power (P_{mpp}) at the maximum power point of the PV array. And the P_{mpp} and V_{mpp} are the input power and voltage of the DC-DC converter in the LWPT system. The decreases of P_{mpp} and V_{mpp} will lead to the decreases of the output power and voltage of the LWPT system. As displayed in Fig. 11, subfigures (a), (b), (c) and (e) depict the same variation trend for P_{mpp} and V_{mpp} with the x-axis parameter, while in (d) and (f), the variation trend is opposite. In Fig. 11(a), the P_{mpp} and V_{mpp} decrease with the increasing C_n^2. That is because the larger the C_n^2 is, the larger the laser intensity attenuation is, which makes the beam

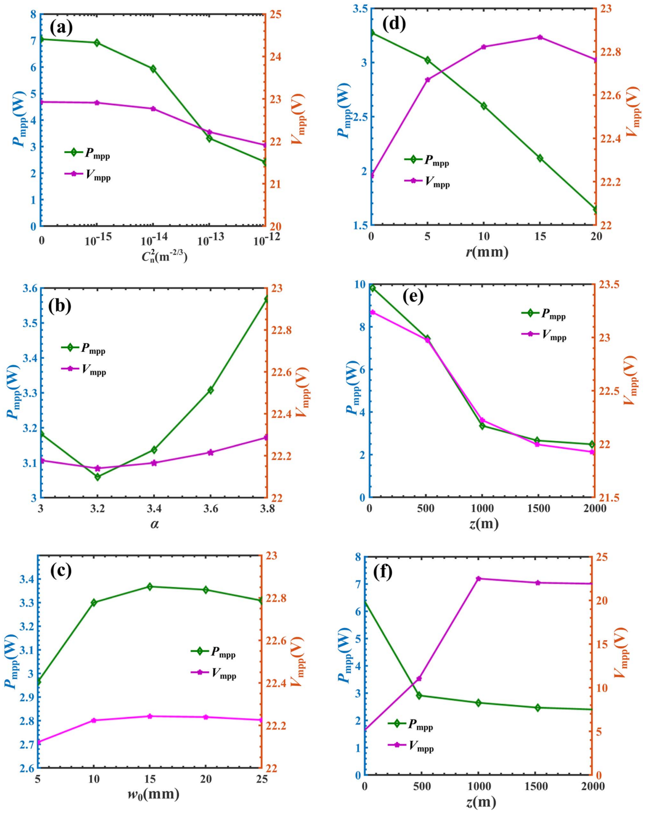

Fig. 11. P_{mpp} and V_{mpp} from the Figs. 6 to 9.

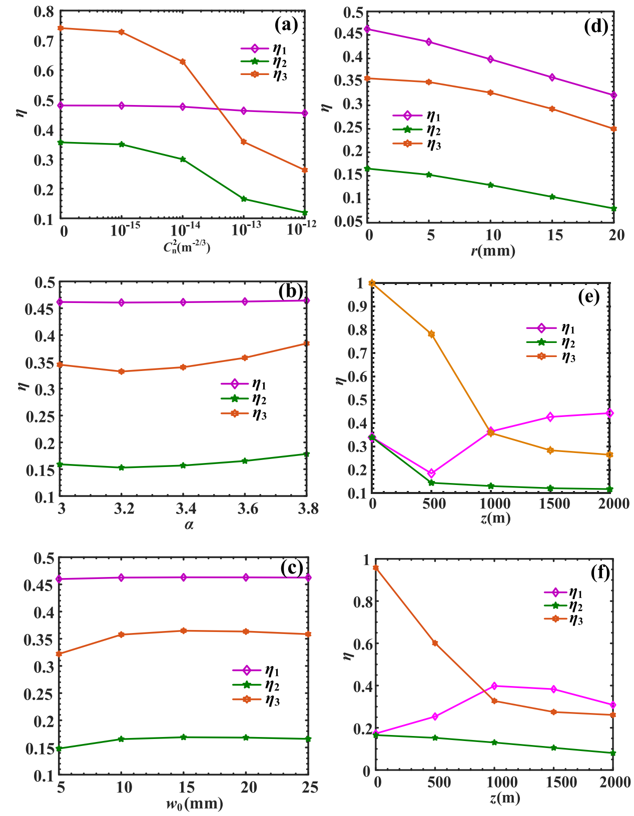

Fig. 12. Efficiency with η_1, η_2 and η_3 corresponding to Fig. 11.

spreading and leads to the decrease of the laser energy received by the PV array. And the trend of laser intensity versus C_n^2 is consistent with that of P_{mpp} and V_{mpp}. In Fig. 11(b), the changes in P_{mpp} and V_{mpp} are due to the change of α and have the similar trends with α. In Fig. 11(c), the P_{mpp} and V_{mpp} initially increase and then decrease with w_0. This phenomenon can be attributed that where the energy incident on the PV array surpasses its absorption and conversion capabilities, thereby leading to energy dissipation when initial beam waist width has a little size. However, excessive waist width will cause the spot area to exceed the PV array area, resulting in the loss of laser energy. In Fig. 11(d), the P_{mpp} decreases with the increase of r (distance of pointing error). When $r = 20$ mm, the attenuation percent of P_{mpp} is 50.9% (from 3.3 W to 1.62 W). And the V_{mpp} initially increases and then decreases, where the change interval is 22.26 V to 22.88 V. Fig. 11(e) shows the changes of P_{mpp} and V_{mpp} with transmission distance z when $\boldsymbol{r} = \mathbf{0}$. For P_{mpp}, the attenuation in 1000 m accounts for 66.7% (from 9.9 W to 3.3 W) of the initial position. The attenuation in 2000 m is 74.8% (from 9.9 W to 2.5 W) of the initial position. This indicates that under the influence of atmospheric turbulence, the change rate of P_{mpp} is larger at short distances than at long distances. The change in V_{mpp} is 1.3 V (from 23.2 V to 21.9 V). In Fig. 11(f), it is observed that the transmission distance has obvious effect on P_{mpp} and V_{mpp} when considering pointing error. P_{mpp} decrease with the transmission distance. The change in V_{mpp} is 17.2 V (from 5.1 V to 22.3 V). Therefore, it is necessary for the DC-DC converter in the LWPT system to have a wide input voltage range and high voltage gain.

In Fig. 12, the η_1, η_2 and η_3 represent the photoelectric conversion efficiency of the PV array, the total efficiency of the initial laser energy to output power of the PV cell and the efficiency of laser transmission in the atmosphere, respectively. Simulation results indicate that the turbulence parameters and initial beam width, as shown in Fig. 12(a), (b) and (c), have little effect on the photoelectric conversion efficiency of PV array when the transmission distance is 1000 m and the beam is not offset. At this time, according to the efficiency η_2, it can be inferred that the efficiency of the system will increase initially and decrease afterwards with the beam waist width w_0. Therefore, when the laser energy is constant, the optimal waist width should be selected based on the actual size of the PV array. From Fig. 12(d), it can be seen that η_1 decreases as the pointing error increases. This is because the pointing error makes the energy distribution on the PV array more uneven, which causes more power loss. The efficiency η_2 descent 51.5% (from 16.5% to 8%) when the pointing error changes from $\boldsymbol{r} = (0\text{ mm}, 0°)$ to $\boldsymbol{r} = (20\text{ mm}, 45°)$. Comparing Fig. 12(e) with Fig. 12(f), it is obvious that the pointing error changes the variation trend of η_1 versus z. η_1 reaches its maximum when the pointing error is $\mathbf{0}$ and the propagation distance is 1000 m. And the pointing error attenuates the overall efficiency η_2 of the system. The η_2 and η_3 decreases as the x-axis parameter increases as shown in Fig. 12(a), (d), (e), and (f). The η_2 and η_3 initially decrease and

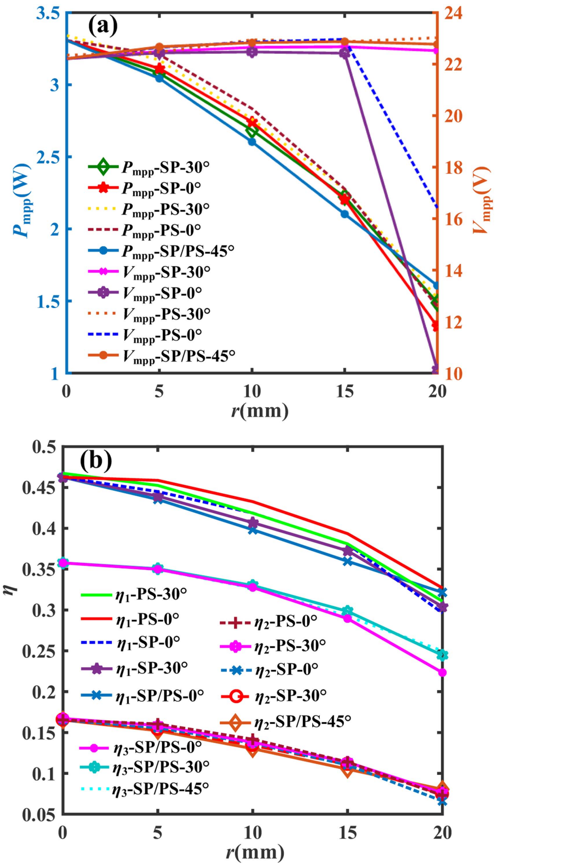

Fig. 13. P_{mpp}, V_{mpp} and efficiency (η_1, η_2 and η_3) versus pointing error (r, θ) and the array configurations. (a) The P_{mpp} and V_{mpp} of the SP and PS PV arrays versus (r, θ); (b) The η_1, η_2 and η_3 of the SP and PS PV arrays. Here, $w_0 = 10$ mm, $C_n^2 = 10^{-13}$ m$^{-2/3}$, $\alpha = 3.6$, $z = 1000$ m.

then increase with the α, which opposite with w_0 in Fig. 12(b) and (c). Comparing Fig. 12(d), (e) and (f), we can find that the photoelectric conversion efficiency η_2 is affected by the pointing error and transmission distance.

Fig. 13 shows the P_{mpp}, V_{mpp} and efficiency of SP and PS arrays at the maximum power point versus pointing error. One can find that the V_{mpp} of SP and PS arrays are attenuated when the angle θ is 0° and the offset distance r is larger than 15 mm. At this time, the V_{mpp} plunges to 10.1 V and 16.4 V for the SP and PS array when $r = 20$ mm, $\theta = 0°$. And the V_{mpp} of the PS array are larger than the SP array. The decrease of the V_{mpp} will result in the decrease of the output voltage of the DC-DC converter. The DC-DC converter cannot supply power to the storage battery and load in the LWPT system, when its output voltage less than the voltage of the storage battery. Therefore, the large pointing error may cause the failure of the LWPT system. The differences between V_{mpp} of the PS array and SP array are less than 0.5 V when the offset distance is within 15 mm. And the V_{mpp} of the PS array and SP array are more than 22 V. In addition, P_{mpp} with different offset angle θ have little difference, but which obviously decrease with the offset distance r. Therefore, the offset distance r of the pointing error will significantly decrease the efficiency of the LWPT system. In Fig. 13(b), the η_1, η_2 and η_3 of the SP array and PS array attenuate as the offset distance r increases. And the difference of the η_1, η_2 and η_3 of the SP array and PS array at the same pointing error is less than 10%, respectively. The main reason is that the beam spreading at 1000 m makes the changes of laser intensity distribution smaller than that within 1000 meters.

IV. Conclusion

In conclusion, this paper presents a study of the output characteristics of the PV array in the LWPT system considering non-Kolmogorov turbulence and pointing error. A theoretical model of the laser intensity and equivalent circuit of the PV array in non-Kolmogorov turbulence is proposed. Further, the output characteristics of the PV array versus the generalized exponent, the generalized structure parameter, atmospheric turbulence, transmission distance, initial beam width and pointing error are studied. The results reveal that the SP array and the PS array have the same output characteristics when the angle of the pointing error is 45°. The P_{mpp} and the system efficiency η_2 descend 50.9% and 51.5%, respectively, when the transmission distance is 1000 m and the pointing error changes from $r = (20$ mm, $45°)$ to $r = (0, 0)$. Moreover, the descend values of P_{mpp} are 66.7% and 74.8% at 1000 m and 2000 m, respectively, when the pointing error $r = (10$ mm, $45°)$. Meanwhile, the V_{mpp} increases significantly (from 5.1 V to 22.3 V) with the increasing of transmission distance. Furthermore, the results also suggest that the system efficiency of the PV array decreases with the increase of the generalized structure parameter, pointing error and transmission distance while less affected by generalized exponent and initial waist width. The simulation results demonstrate that turbulence and pointing error will cause the output voltage and power of the PV array attenuation. And the *P-V* characteristic curve of the PV array will present multi-peaks. Which will not only result in the decrease of the output voltage and power or failure of the LWPT system, but also have negative effects on the stability. The findings of this study have significant implications for the optimization of the overall structure of LWPT systems especially the design of PV array and DC-DC converter.

Appendix

When $\kappa\xi|\boldsymbol{\rho}_1 - \boldsymbol{\rho}_2| << 1$, $J_0(\kappa\xi|\boldsymbol{\rho}_1 - \boldsymbol{\rho}_2|)$ can be approximated to the first two terms in the power series expansion [26], i.e.,

$$J_0(\kappa\xi|\boldsymbol{\rho}_1 - \boldsymbol{\rho}_2|) \approx 1 - \frac{1}{4}(\kappa\xi|\boldsymbol{\rho}_1 - \boldsymbol{\rho}_2|)^2 \tag{A-1}$$

Assuming

$$\boldsymbol{I}_t = \left\{ -\frac{\pi^2 k^2 z}{3} \int_0^\infty \kappa^3 \Phi_n(\kappa, \alpha) d\kappa \right. \tag{A-2}$$

after some tedious mathematical manipulation, the term $\boldsymbol{I}_t$ is expressed as [27]

$$\boldsymbol{I}_t = -\frac{\pi^2 k^2 z}{3} A(\alpha) C_n^2 / [2(\alpha - 2)] \cdot \left[\beta\kappa_m^{2-\alpha} \exp\left(\kappa_0^2/\kappa_m^2\right) \Gamma\left(2 - \alpha/2, \kappa_0^2/\kappa_m^2\right) - 2\kappa_0^{4-\alpha}\right] \tag{A-3}$$

Then, we rewrite (2) by using (A-1)

$$I(\boldsymbol{\rho}, z) = \left(\frac{k}{2\pi z}\right)^2 \iint d^2\boldsymbol{\rho}_1 \iint d^2\boldsymbol{\rho}_2 \exp\left(-\frac{\boldsymbol{\rho}_1^2 + \boldsymbol{\rho}_2^2}{w_0^2}\right) \times \exp\left\{\frac{ik}{2z}\left[(\boldsymbol{\rho} - \boldsymbol{\rho}_1)^2 - (\boldsymbol{\rho} - \boldsymbol{\rho}_2)^2\right]\right\} \times \exp\left\{-\frac{\pi^2 k^2 z}{3}(\boldsymbol{\rho}_1 - \boldsymbol{\rho}_2)^2 \int_0^\infty \kappa^3 \Phi_n(\kappa, \alpha) d\kappa\right\} \tag{A-4}$$

Introducing two variables of integration $\boldsymbol{\rho_S} = (\boldsymbol{\rho}_1 + \boldsymbol{\rho}_2)/2$, $\boldsymbol{\rho_T} = \boldsymbol{\rho}_2 - \boldsymbol{\rho}_1$, where $\boldsymbol{\rho}_S = (s_x, s_y)$, $\boldsymbol{\rho}_T = (t_x, t_y)$, the formula can be rewritten as

$$I(\boldsymbol{\rho}, z) = \left(\frac{k}{2\pi z}\right)^2 \iint \iint ds_x dt_x ds_y dt_y \times \exp\left[-\frac{2s_x^2 + t_x^2/2}{w_0^2}\right] \times \exp\left[-\frac{2s_y^2 + t_y^2/2}{w_0^2}\right] \times \exp\left\{\frac{ik}{z}(xt_x - s_x t_x + yt_y - s_y t_y)\right\} \times \exp\left\{-\frac{\pi^2 k^2 z}{3} \int_0^\infty \kappa^3 \Phi_n(\kappa, \alpha) d\kappa \left(t_x^2 + t_y^2\right)\right\} \tag{A-5}$$

According to the integral formula

$$\int \exp(-p^2 x^2 + qx) dx = \frac{\sqrt{\pi}}{p} \exp\left(\frac{q^2}{4p^2}\right) \tag{A-6}$$

and after tedious integral calculations, the average intensity in (5) can be obtained.

Disclosures: The authors declare no conflicts of interest.

References

[1] L. Summerer and O. Purcell, "Concepts for wireless energy transmission via laser," in *Proc. Int. Conf. Space Opt. Syst. Appl.*, Jan. 2009, pp. 1–9.

[2] J. Fakidis, S. Videv, S. Kucera, H. Claussen, and H. Haas, "Indoor optical wireless power transfer to small cells at nighttime," *J. Lightw. Technol.*, vol. 34, no. 13, pp. 3236–3258, Jul. 2016.

[3] C. Zhang, W. Zhong, X. Liu, and S. Y. R. Hui, "A fast method for generating time-varying magnetic field patterns of mid-range wireless power transfer systems," *IEEE Trans. Power Electron.*, vol. 30, no. 3, pp. 1513–1520, Mar. 2015.

[4] K. Jin and W. Zhou, "Wireless laser power transmission: A review of recent progress," *IEEE Trans. Power Electron.*, vol. 34, no. 4, pp. 3842–3859, Apr. 2019.

[5] S. V. Chong, G. Williams, J. Kennedy, F. Fang, J. Tallon, and K. Kadowaki, "Large low-temperature magnetoresistance in $SrFe_2As_2$ single crystals," *EPL Europhysics Lett.*, vol. 104, no. 1, Oct. 2013, Art. no. 17002.

[6] Y. Zhang, Y. Wang, S. Yang, and C. Zhao, "Evaluation of impacts of laser parameters on laser cells efficiencies," in *Proc. SPIE*, vol. 9619, Aug. 2015, Art. no. 961904.

[7] M. Xian-Long, L. Bei, C. Lopez, and C.-L. Liu, "Multi-field coupling characteristics of photovoltaic cell under non-uniform laser beam irradiance," *Sustain. Energy Technol. Assess.*, vol. 52, Aug. 2022, Art. no. 101963.

[8] G. Li, Y. Lu, Q. Xuan, G. Pei, J. Ji, and X. Zhao, "Performance analysis on a crystalline silicon photovoltaic cell under non-uniform illumination distribution with a high electrical efficiency," *Sol. Energy*, vol. 203, pp. 275–283, Jun. 2020.

[9] O. Bingol and B. Ozkaya, "Analysis and comparison of different PV array configurations under partial shading conditions," *Sol. Energy*, vol. 160, pp. 336–343, Jan. 2018.

[10] W. Zhou and K. Jin, "Optimal photovoltaic array configuration under gaussian laser beam condition for wireless power transmission," *IEEE Trans. Power Electron.*, vol. 32, no. 5, pp. 3662–3672, May 2017.

[11] P. Sprangle, B. Hafizi, A. Ting, and R. Fischer, "High-power lasers for directed-energy applications," *Appl. Opt.*, vol. 54, no. 31, pp. F201–F209, Nov. 2015.

[12] G. Gbur and E. Wolf, "Spreading of partially coherent beams in random media," *J. Opt. Soc. Amer. A: Opt. Image Sci., Vis.*, vol. 19, no. 8, pp. 1592–1598, Aug. 2002.

[13] H. Tang, B. Ou, B. Luo, and H. Guo, "Average spreading of a radial Gaussian beam array in non-Kolmogorov turbulence," *J. Opt. Soc. Amer. A Opt. Image Sci. Vis.*, vol. 28, no. 6, pp. 1016–1021, 2011.

[14] I. Toselli, L. C. Andrews, R. L. Phillips, and V. Ferrero, "Angle of arrival fluctuations for free space laser beam propagation through non-kolmogorov turbulence," in *Proc. SPIE*, vol. 6551, pp. 149–160, 2007.

[15] X. Liu, F. Wang, C. Wei, and Y. Cai, "Experimental study of turbulence-induced beam wander and deformation of a partially coherent beam," *Opt. Lett.*, vol. 39, no. 11, pp. 3336–3339, 2014.

[16] A. Zilberman, E. Golbraikh, N. S. Kopeika, and A. Virtser, "Lidar study of aerosol turbulence characteristics in the troposphere: Kolmogorov and non-kolmogorov turbulence," *Atmospheric Res.*, vol. 88, no. 1, pp. 66–77, 2008.

[17] R. R. Beland, "Some aspects of propagation through weak isotropic non-Kolmogorov turbulence," in*Proc. SPIE*, vol. 2375, pp. 6–16, Apr. 1995.

[18] I. Toselli, L. C. Andrews, R. L. Phillips, and V. Ferrero, "Frees-pace optical system performance for laser beam propagation through non-Kolmogorov turbulence for uplink and downlink paths," in *Proc. SPIE*, vol. 6708 Sep. 2007, Art. no. 670803.

[19] T. Shirai and T. Asakura, "Spectral changes of light induced by scattering from spatially random media under the Rytov approximation," *J. Opt. Soc. Amer. A*, vol. 12, no. 6, pp. 1354–1363, 1995.

[20] D. Liu, H. Yin, and G. Wang, "Propagation of partially coherent Lorentz–Gauss vortex beam through oceanic turbulence," *Appl. Opt.*, vol. 56, no. 31, pp. 8785–8792, 2017.

[21] X. Ji and B. Lü, "Turbulence-induced quality degradation of partially coherent beams," *Opt. Commun.*, vol. 251, no. 4–6, pp. 231–236, 2005.

[22] A. E. Siegman, "How to (Maybe) measure laser beam quality," in *DPSS (Diode Pumped Solid State) Lasers: Applications and Issues* (OSA Trends in Optics and Photonics), vol. 17, M. Dowley, Ed. Washington, DC, USA: Optica Publishing Group, 1998, Paper MQ1.

[23] Z. Yang, Y. Song, Z. Duan, and T. Wang, "New sigmoid-like function better than Fisher z transformation," *Commun. Statist.: Theory Methods*, vol. 45, no. 7/8, pp. 2332–2341, 2016.

[24] S. S. Li, *Semiconductor Physical Electronics*. New York, NY, USA: Springer, 2006.

[25] D. A. Neamen, "*Semiconductor Physics and Devices: Basic Principles*. New York, NY, USA: McGraw-Hill, 2012.

[26] L. Lu, Z. Wang, and J. Zhang, "Average intensity of M×N Gaussian array beams in oceanic turbulence," *Appl. Opt.*, vol. 54, no. 25, pp. 7500–7507, 2015.

[27] G. Wu, H. Guo, S. Yu, and B. Luo, "Spreading and direction of Gaussian-Schell model beam through a non-Kolmogorov turbulence," *Opt. Lett.*, vol. 35, no. 5, pp. 715–717, 2010.